Applied Catalysis B: Environmental 237 (2018) 996–1002

Contents lists available at ScienceDirect

Applied Catalysis B: Environmental

journal homepage: www.elsevier.com/locate/apcatb

Impact of structural defects and hydronium ion concentration on the stability of zeolite BEA in aqueous phase

Sebastian Prodinger[a], Hui Shi[a], Huamin Wang[a], Miroslaw A. Derewinski[a,*], Johannes A. Lercher[a,b,*]

[a] Institute for Integrated Catalysis, Pacific Northwest National Laboratory, P.O. Box 999, Richland, WA, 99352, United States
[b] Department of Chemistry and Catalysis Research Institute, TU München, Lichtenbergstrasse 4, 85748 Garching, Germany

ARTICLE INFO

Keywords:
Zeolite stability
Hot liquid water
Defects
Fluoride method
Hydrophobization

ABSTRACT

The presence of fluoride anions in the synthesis gel leads to zeolite BEA with high hydrothermal stability. This longer lifetime is caused by a lower concentration of internal silanol defects that are sites of the initial framework hydrolysis eventually destroying the lattice structure. The lifetime of these zeolites was the higher the lower the concentration of framework bridging hydroxyl groups that form hydronium ions was. While lattice hydrolysis was initiated at defect sites in all cases, the role of defects became less important as the concentration of hydronium ions increased. At higher concentration of hydrated hydronium ions, the presence of water associated with the hydrated hydronium ions limits the useful lifetime of zeolite catalysts in water. For such materials, the selective hydrophobization of the external surface extends the lifetime.

1. Introduction

Zeolites are tectosilicates for which the voids in the structure (pores) are an integral part of the crystal structure. Incorporation of heteroatoms such as Al results in the generation of charge in the lattice that has to be balanced by metal cations or H^+, leading to Brønsted acid sites in case of the latter [1,2]. This has enabled the effective use of these materials as shape selective catalysts in gas and liquid phase reactions.

The surprisingly high catalytic activity in aqueous phase has induced significant interest [3–5]. Resembling the dimensions of enzyme pockets, zeolite confines were shown to confer a unique steric environment to hydronium ions, enhancing their catalytic activities beyond that found for hydronium ions in unconstrained environments [6,7]. However, the stability of zeolites in these aqueous phase reactions has proven to be a major challenge [8–10]. In contrast to the relatively good stability of zeolites against steaming, their metastable framework tends to disintegrate in hot liquid water.

The reason for this limited stability lies in the solubility of silica. A first impression of the impact of the mode of termination and a better understanding of the potential stabilization can be obtained by comparing the dissolution rates of amorphous silica and quartz [11]. The significantly slower dissolution of quartz compared to amorphous silica has been associated with the lower concentration of SiOH groups in quartz [11,12]. By analogy, the dissolution rate of zeolites in hot liquid water was correlated with the concentration of SiOH groups terminating crystal domains and defects in the framework [13,14]. These defects are mostly incomplete linkages in the zeolite or in the incomplete retention of heteroatoms during thermal treatment after synthesis such as in the calcination to remove organic structure directing agents [15–17]. In the case of zeolite BEA, a dominant intergrowth between polymorphs A and B leads to an additional source of structural defects [17]. Particle size and morphology affect the SiOH concentration on the exterior surface.

To minimize hydrolytic degeneration of the framework, strategies focused primarily on reduction of SiOH group concentrations by chemical functionalization [14,18]. This has led to promising results for biphasic alkylation [18], as well as the aqueous phase dehydration of alcohols [19].

It has been found, however, that the stability of zeolites does not only depend on the concentration of defects. Only at low concentrations of acid sites was framework hydrolysis directly related to the concentration of structural defects [19]. At higher concentrations of tetrahedral aluminum, the stability was related to the concentration of hydrated hydronium ions [19]. We hypothesized that the increasing concentration of intra-porous water caused by the very stable hydrated hydronium ions kinetically enhanced framework hydrolysis.

In order to probe this hypothesis, we prepared a series of materials with low defect concentrations, to explore the impact of hydrated hydronium ions on catalyst lifetime. Synthesis of zeolite BEA in presence of fluoride anions was used to minimize connectivity defects by charge

* Corresponding authors at: Institute for Integrated Catalysis, Pacific Northwest National Laboratory, P.O. Box 999, Richland, WA, 99352, United States.
E-mail addresses: miroslaw.derewinski@pnnl.gov (M.A. Derewinski), Johannes.Lercher@pnnl.gov (J.A. Lercher).

https://doi.org/10.1016/j.apcatb.2018.06.065
Received 11 April 2018; Received in revised form 19 June 2018; Accepted 25 June 2018
Available online 28 June 2018

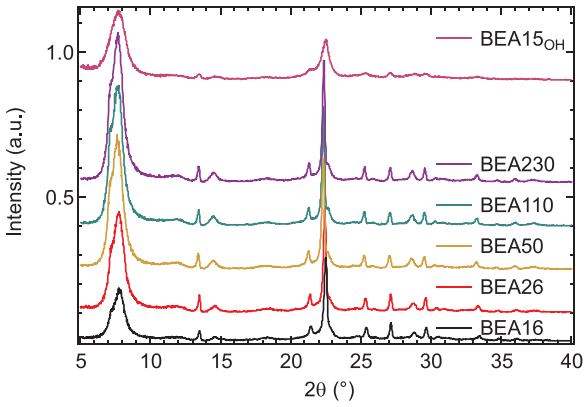

Fig. 1. X-ray diffraction of BEA synthesized in F^- and OH^- medium. All reflections match those associated with BEA type framework.

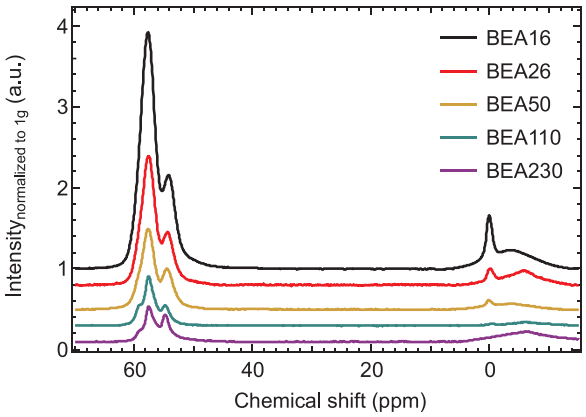

Fig. 2. ^{27}Al MAS NMR (bottom) shows the state of the tetrahedral Al (54–59 ppm) and octahedral EFAl (5 to −10 ppm) in the framework.

compensating the structure directing agent. The inherently slow crystal growth leads furthermore to relatively large particles that minimize crystallite terminating SiOH groups.

2. Results and discussion

2.1. Physicochemical characterization of BEA synthesized in fluoride media

Zeolite BEA was synthesized with Si/Al ratios ranging from 16 to 230. X-ray diffraction (XRD) characterization of the calcined materials in Fig. 1 shows diffraction peaks characteristic of fully crystalline BEA materials. Compared to BEA synthesized in OH^- rich medium ($BEA15_{OH}$), all peaks were better resolved, which is attributed to a larger crystallite size as well as a reduced defect concentration [16].

The asymmetry of the low angle diffraction peak at *2θ* of 7–8° suggests an enrichment of polymorph A [16], compared to the 50/50 mixture obtained in OH^- rich media. In addition, the peak at *2θ* of 22.4° is significantly narrower than for BEA synthesized in alkaline medium, which indicates a larger crystallite size [20].

As mentioned above, the size of the crystals synthesized in F^- containing medium (Fig. S1) was larger than a few µm over the whole Si/Al range. The Al-rich BEA16 and BEA26 had the largest average particle diameters (8–9 µm). This largest average particle diameter is hypothesized to be caused by the longer synthesis time required to reach full crystallinity with higher concentrations of Al (Table S1). The zeolite particles were isolated and nearly devoid of intercrystalline mesoporosity (0.04 - 0.06 cm^3/g; Table S2 and Fig. S2), while zeolite BEA synthesized in an alkaline medium had a significant degree of mesoporosity [19].

The concentrations of Brønsted acid sites (BAS) and tetrahedral Al were determined by IR spectroscopy of adsorbed pyridine (Table 1) and ^{27}Al MAS NMR (Fig. 2), respectively. A good agreement between the concentrations of BAS and of tetrahedral Al was observed, indicating the absence of distorted tetrahedral Al species and compensation by aluminum containing cations [21].

Up to three peaks were observed in ^{27}Al MAS-NMR spectra (tetrahedral region, 54–59 ppm), reflecting the different chemical environments of the 9 Al T-sites in the BEA framework [22]. The majority of as-synthesized zeolites did not have a noticeable concentration of octahedral extra-framework Al (EFAl, 5 to −10 ppm) (Fig. S4). Calcination led to a removal of tetrahedral framework Al and resulted in varying concentrations of octahedral EFAl (Fig. 2). The EFAl species in BEA16, BEA26, and BEA50 are characterized by a narrow peak at 0 ppm and a broad from 5 to – 10 ppm, whereas high-silica BEA showed only a rather broad peak. The narrow peak for octahedrally coordinated Al is attributed to the highly symmetric hexaquo complex of Al, reducing its quadrupolar moment [23].

The broad peak in the ^{27}Al MAS-NMR spectra is attributed to highly distorted EFAl species, as typical for AlO_x clusters [23]. While the concentration of octahedral Al was 15–19% for BEA16 – BEA110, the BEA230 sample contained 45% octahedral Al. We hypothesize that the significant concentration of octahedral EFAl in BEA230 is a result of a lower degree of Al incorporation. Indeed, ^{27}Al MAS NMR of the as-synthesized BEA230 shows the pronounced presence of a distorted octahedral EFAl species at 13 ppm accounting for 21% of the total Al signal, specifically attributed to an Al-fluoro complex (Fig. S4) [25]. After calcination, these EFAl species are transformed into the highly distorted AlO_x clusters giving rise to the signal between 5 and – 10 ppm. The distribution of the Al in the crystallites was found to be largely homogenous as indicated by comparable Si/Al ratios obtained with surface sensitive EDX analysis as well from bulk ICP-AES methods (see Table S1 for Si/Al comparison).

Table 1
Spectroscopic characterization of a range of BEA zeolite synthesized in the presence of F^- anions as well as one sample ($BEA15_{OH}$) synthesized in OH^- medium for comparison.

Sample	Al_{ICP}[a] (µmol/g)	Al_{NMR}[b] (µmol/g)	Tetrahedral Al^{3+} (µmol/g)	Octahedral Al^{3+} (µmol/g)	Brønsted acid sites[c] (µmol/g)	Lewis acid sites[c] (µmol/g)	Defect sites[d] (µmol/g)
BEA16	985	990	802	188 (19%)	915	270 (23%)	210 ± 24
BEA26	620	590	480	110 (18%)	555	105 (16%)	185 ± 23
BEA50	330	320	265	55 (17%)	260	74 (22%)	150 ± 21
BEA110	165	130	110	20 (15%)	115	25 (18%)	80 ± 12
BEA230	75	110	60	50 (45%)	50	12 (19%)	45 ± 10
$BEA15_{OH}$	1120	910	675	235 (26%)	540	415 (43%)	380 ± 50

[a] ICP-AES performed to determine elemental composition, ± 10%.
[b] referenced to a calibration curve with Al content determined with ICP-AES, ± 10%.
[c] quantification with pyridine adsorption after outgassing at 150 °C, ± 10%.
[d] difference method [24] using ^{29}Si and ^{27}Al MAS NMR.

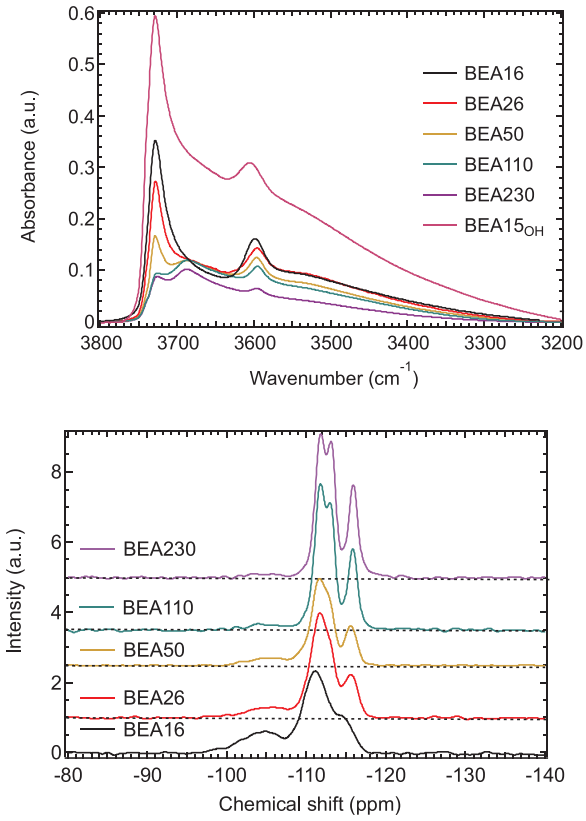

Fig. 3. (Top panel) Infrared spectroscopy of the hydroxyl region (3200–3800 cm^{-1}) of calcined BEA synthesized in fluoride and hydroxide ($BEA15_{OH}$) media. The spectra are acquired at 450 °C after evacuating for 1 h. All spectra are normalized to the lattice overtones between 1740 and 2090 cm^{-1} (not shown). Color-coding is reported in the legend. (Bottom panel) Quantitative ^{29}Si MAS NMR spectra of calcined BEA zeolite. The peak at −105 ppm corresponds to Q^3 species, whereas both peaks at −111 and −116 ppm correspond to Q^4 species. Dashed lines represent the baseline. Color-coding is reported in the legend.

2.2. Nature and concentration of defect sites

The IR spectra of the bands of the OH groups terminating lattice defects are compiled in Fig. 3. The strong band at 3735 cm^{-1} is attributed to SiOH groups in the zeolite pores generated by defects [26]. External SiOH (3745 cm^{-1}) were only observed as a shoulder in $BEA15_{OH}$ [27]. This points to a larger concentration of OH groups, in line with the smaller particle size of this sample. As the defect concentration in the hydroxide synthesis route increases with the Si/Al ratio [19], the IR spectra in Fig. 4 highlight the effectiveness of reducing internal defect formation via synthesis in F-containing media. The decreasing intensity of the band at 3735 cm^{-1} points to a decreasing concentration of defects for the high-silica materials.

In passing it should be noted that the band at 3690 cm^{-1} in the IR spectra of high-silica BEA is assigned to weakly hydrogen-bonded SiOH groups rather than Al—OH vibrations from EFAl [28]. As the temperature increased and residual water desorbed this band shifted towards higher wavenumbers indicating a weaker hydrogen bonding (Fig. S5). Additionally, this band is present even in purely siliceous BEA (not shown), and has been observed in Al-free Ti-BEA [28].

Without knowledge of the molar extinction coefficients of the various hydroxyl bands in Fig. 3, the quantification of the defect concentration is not possible. The concentration of defect sites was, therefore, quantified using Bloch-decay ^{29}Si MAS NMR, which is characteristic of the Si-O-Si connectivity in the zeolite framework. Two species of Si were differentiated (Fig. 4, bottom), Si surrounded by 4 Si,

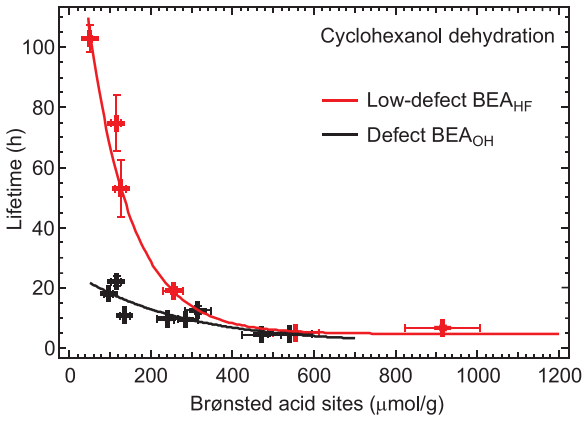

Fig. 4. Correlation between the zeolite lifetime and the concentration of Brønsted acid sites in BEA zeolites. The latter corresponds to the concentration of hydronium ions and affects that of intraporous water. Color-coding is reported in the legend. The Defect BEA samples were reported previously [19] and are reprinted with permission from Prodinger, S.; Shi, H.; Eckstein, S.; Hu, J. Z.; Olarte, M. V.; Camaioni, D. M.; Derewinski, M. A.; Lercher, J. A., *Chem. Mater.* **2017**, 29, (17), 7255–7262. Copyright 2017 American Chemical Society.

i.e., $Si(OSi)_4$ (Q^4) (– 109 to – 118 ppm) and Si connected to only 3 Si and one heteroatom (Q^3) (– 100 to – 108 ppm) [29,30]. The Q^3 Si can be further differentiated as $(SiO)_3SiOAl$ or $(SiO)_3SiOH$, the latter giving rise to the defect concentration (SiOH). As the Si/Al ratio increased, the resolution of the peaks also improved, which is attributed to the increased structural order in the system [16,31]. With decreasing Al concentration, the peaks also shifted upfield as the shielding increased. At higher Si/Al, the contribution of the Q^3 peak (−100 to −108 ppm) was reduced. Knowing the exact concentration of framework Al (SiOAl, −106 ppm) by subtracting the amount of EFAl (quantified by ^{27}Al MAS NMR, Fig. 2) from the total Al as determined via elemental analysis, allows us to extract the concentration of SiOH (– 103 ppm) from the Q^3 signal in the ^{29}Si MAS NMR [24,30]. The defect concentration for BEA synthesized via the fluoride route decreased from 210 to 45 μmol/g, or 0.81–0.17 defect per unit cell, with increasing Si/Al ratios (Table 1 and Fig. S7). This is significantly lower than the value of 1100 μmol/g determined for defective high-silica BEA synthesized in alkaline-medium [19] or the 380 μmol/g value for the $BEA15_{OH}$, confirming that the fluoride route generates much fewer lattice defects. We speculate the residual defect concentration to arise from dealumination during the calcination of the OSDA as well as from the intergrowth between polymorphs A and B, where the lattice mismatch is terminated with SiOH groups [17].

2.3. Catalytic activity and stability

Aqueous phase cyclohexanol dehydration is used as typical example of an acid catalyzed step in hydrodeoxygenation of phenolic compounds [32]. It is catalyzed by hydrated hydronium ions. For zeolites, the concentration of such hydronium ions is equivalent to that of Brønsted acid sites generated by the tetrahedral substitution in the lattice. Using alcohol dehydration, we showed previously that the presence of an organic substrate (cyclohexanol) leads to a prolonged lattice integrity of BEA zeolites compared to the timespan stable in pure liquid water [19].

The initial rates, the rates normalized by the concentration of hydronium ions (turnover frequencies, TOF), as well as TON [33] (the moles of substrate that a mol of catalyst can convert up to the point of complete deactivation) are listed in Table S3. The TOFs were all within a factor of 2, indicating that the environment of the active site, the hydronium ion, remains nearly unchanged irrespective of the Si/Al changes.

For the majority of cases, the reaction was performed until the

conversion ceased (Fig. S8). For BEA110 and BEA230, reduction in rate of conversion was also appreciable, but the conversion persisted even after 100 h. Because the reaction in zeolite BEA was of zero order in cyclohexanol beyond concentrations of 0.1 M [7], the observed reduction in rate is concluded not to be caused by depletion of reactants, but by decay of the zeolite. The conversion-time curves (Fig. S8) were fitted with an exponential decay function, to obtain the lifetime of the zeolite by extrapolation. These lifetimes are plotted in Fig. 4 against the corresponding concentration of Brønsted acid sites.

The attainable lifetime of zeolite BEA synthesized via the fluoride route (BEA_{HF}) is in general longer than that with the samples synthesized in the OH^- medium, especially for high Si/Al ratios. As the concentration of hydronium ions increases, the difference in lifetime between the two series of BEA zeolites is reduced.

Note that the Al-rich $BEA15_{OH}$ had a defect concentration of 380 µmol/g, i.e., almost twice that of the BEA16 (210 µmol/g) obtained via the fluoride route. This suggests that beyond a certain concentration of aluminum in the lattice, i.e., a certain concentration of hydrated hydronium ions, lower concentrations of defects do not lead to a measurable increase in lifetime. We hypothesize, thus, that either the hydronium ion itself or the induced higher concentration of water in the pores strongly influences the lattice stability.

It is striking to see that the concentration of adsorbed water in BEA_{HF} catalysts correlates with the BAS concentration in a strictly linear fashion. In zeolite BEA synthesized in hydroxide media, the high concentration of defect sites led to a significant increase in the concentration of adsorbed water (Fig. 5, black squares). We previously established for BEA_{OH} that defect sites bind up to 8 molecules of water [19]. Therefore, the negligible contribution of water adsorption on defect sites in the low-defect BEA_{HF} is attributed to a different nature of defect sites, namely isolated OH groups at the polymorph intergrowths as opposed to hydroxyl nests in highly defective BEA_{OH}.

2.4. Factors contributing to zeolite lifetime

Overall, the rate of catalyst decay appears to be a function of water concentration in the zeolite pores [19,34]. As the chemical potential of water (the main constituent of the liquid immersing the zeolite) is identical inside and outside of the pores under equilibrium conditions, we tentatively conclude that either the framework dissolution is transport limited or the higher concentration of water influences the entropic term in the dissolution rate constant (Fig. 6).

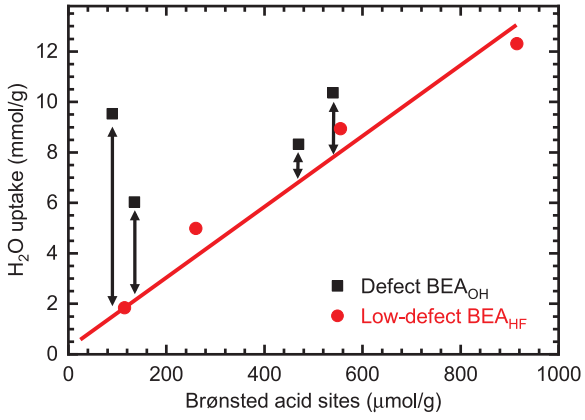

Fig. 5. Intraporous water concentration as determined by measuring the uptake of cyclohexanol from an aqueous solution. The red line shows the correlation between adsorbed water and Brønsted acid sites for BEA synthesized via the fluoride route. Significant amounts of defects lead to increased water uptake as shown by the black marks. Part of the data (Defect BEA_{OH}) was previously reported [19]. Reproduced with permission from Prodinger, S.; Shi, H.; Eckstein, S.; Hu, J. Z.; Olarte, M. V.; Camaioni, D. M.; Derewinski, M. A.; Lercher, J. A., *Chem. Mater.* **2017**, 29, (17), 7255–7262. Copyright 2017 American Chemical Society.

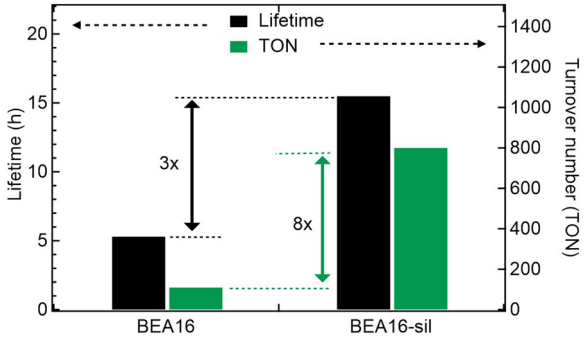

Fig. 6. Side-by-side comparison of lifetimes and apparent turnover numbers obtained for parent and surface modified materials (10 mg).

If transport limitations were the dominating effect, we hypothesized that larger particles would lead to a higher stability. In the gas phase, it is generally accepted that larger particles exhibit a higher hydrothermal stability [35,36]. In the condensed phase and in the presence of hot liquid water, we have previously seen that a defect-rich, high-silica BEA (Si/Al > 75) of roughly 1 µm particle diameter yields a longer lifetime than a respective zeolite of similar chemical properties, but having a smaller particle diameter [19]. Investigating this effect for the Al-rich regime (Si/Al < 50), it is possible to directly compare micrometer sized BEA synthesized via the fluoride route and the smaller hydroxide counterpart (< 300 nm). Interestingly, the catalyst lifetime is not impacted by differing particle sizes (Fig. 4). This indicates that mass transport likely does not play a significant role, pointing to the importance of intrinsic differences in the rate constant of hydrolysis as a function of hydronium ion concentration.

As it has been shown that with low-defect BEA, catalyst lifetime is inversely related to the concentration of hydronium ions, we explored options to stabilize Al-rich BEA. We investigated, therefore, a post-synthetic approach for stabilization by silylating external zeolite particle surfaces using long-chain alkyl-chlorosilanes [18].

The use of a bulky silane, octadecyltrichlorosilane (C_{18}-$SiCl_3$), which cannot enter the pore, leads to its anchoring on the external surface. This modification does not cause a loss of micropores and only a small reduction in BAS concentration is observed. Grafting of the alkyl chains at the outer surface was confirmed by the presence of C—H stretching vibrational bands in the IR spectrum of the modified samples (Fig. S9). This was hypothesized to induce mass transport limitations by preventing the diffusion of water into the pores.

The modification led to a very efficient catalyst which drove the conversion to equilibrium (71%, as verified by increasing the catalyst amount) within ~12 h. As the equilibrium was attained before full deactivation, it was not possible to determine the lifetime of this sample under the same conditions used for other samples, i.e., 30 mg of catalyst in 80 of mL H_2O (1:2600 g/mL). Therefore, alcohol dehydration in water was repeated with a smaller amount of solid catalyst (10 mg, 1:8000 g/mL), which led to the complete dissolution and deactivation of the silylated BEA16 after 15 h (before reaching reaction equilibrium). At the same catalyst/liquid ratio (1:8000 g/mL), the unmodified sample stopped converting alcohols after only 5 h, indicative of its much lower stability. The apparent TON on the hydrophobized BEA16 was 8 times higher than the TON on the parent BEA16 (Table S5). The lifetime (and TON) determined this way depend on the mass of zeolite, because the time required to reach full dissolution of a given material in hot liquid water increases with the solid mass present in the reactor volume. Therefore, comparison of lifetime and TON is only meaningful when the same mass of solid is used for different samples.

Somewhat unexpectedly, the measured TOF of the non-modified BEA16 decreased by more than a factor of 2 when lowering the catalyst loading from 30 to 10 mg, while the externally hydrophobized zeolite

maintained a comparable TOF at a reduced catalyst loading of 10 mg (Table S5). It is important to realize that even though the use of 10 mg zeolite sample facilitated the comparison of stability as shown above, there was one unintended consequence for the calculation of TOFs, due to inevitable partitioning of hydronium ions inside and outside the pores (in the solution) in the absence of significant barriers for water diffusion and proton transfer. Specifically, the calculations of TOFs are based on the assumptions that all hydronium ions are localized in the pores, whereas the solution was slightly acidic (pH < 5), indicating that some hydronium ions initially in the pores of BEA16 are present in the solution at equilibrium.

As hydronium ions in the aqueous phase (unconstrained environment) are at least an order of magnitude lower in catalytic activity for cyclohexanol dehydration than BEA zeolite (constrained environment) [6,7], the measured TOF measured at 10 mg reactor loading of BEA16 would, thus, be significantly lower than the intrinsic TOF of BEA16 and also the TOF measured for 30 mg of zeolite loading (for which relatively much less hydronium ion was partitioned into the solution), as was observed. In contrast, for the BEA16-sil zeolite added at both reactor loadings, there appears to be a much smaller fraction of zeolite associated hydronium ions directly accessible in the solution phase.

The concentration of defects remained largely unchanged by the hydrophobization of the external surface, indicating that the influence of defects on the stability in the Al-rich regime is indeed negligible. While it could be postulated that the capping of external SiOH eliminates a dissolution process starting at the exterior, we consider this an unlikely scenario owing to negligible differences in lifetimes based on particle size (i.e. differing concentrations of external SiOH). The finding of different TOFs for unmodified and hydrophobized zeolites, leads us to conclude that the deposition of long-chain alkyl groups successfully markedly influences the diffusion of water into the zeolite pores (and vice versa the diffusion of hydronium ions into the bulk solution), thus, retarding the dissolution rate.

3. Conclusion

Previous studies have shown a good correlation between Brønsted acid sites or hydrated hydronium ions and zeolite lifetime in aqueous phase reactions with a lower defect concentration additionally aiding in the lifetime of high-silica (Si/Al > 100) zeolites [19]. To conclusively determine and deconvolute the role of defects and hydronium ions on materials of Si/Al < 50 we successfully synthesized BEA zeolite via the fluoride route. This leads to highly crystalline and low defect materials across a wide range of Si/Al ratios. Quantitative comparison with defect-rich materials synthesized in aqueous alkaline medium shows that the impact of increasing hydrophilicity on Al-rich samples offsets framework-stabilizing factors such as lower defect concentrations and larger particle sizes. The results demonstrate the significance of the nature of the external surface. To achieve a durable and efficient Al-rich BEA zeolite, hydrophobization with long-chain alkyl groups was necessary. It led to an improved lifetime and activity, presumably by retarding the diffusion of liquid water into the pores (increasing the lifetime) as well as hydronium ions into the bulk solution (preventing a loss of intrinsic activity).

4. Experimental section

4.1. Chemicals

Octadecyltrichlorosilane (Sigma-Aldrich, > 90%) Cyclohexanol (Sigma-Aldrich, 99%), cyclohexene (Sigma-Aldrich, 99%, GC-grade), 1,3-dimethoxy-benzene (Sigma-Aldrich, 99%), dichloromethane (Sigma-Aldrich, HPLC grade), and sodium sulfate (Acros Organics, 99%, anhydrous) are used as received without further purification.

4.2. Zeolite synthesis of BEA

Al-BEA with Si/Al ratios ranging from 15 to 230 were synthesized in the presence of fluoride anions according to a procedure developed by Camblor et al. [16] An intergrowth between polymorph A and polymorph B results in a disordered structure [37]. The gel composition was as follows SiO_2: xAl_2O_3:(0.54 + 2x)TEAOH:(0.54 + 2x)HF:(7 + 2x) H_2O. Synthesis times are reported in Table S1. Switching from hydroxyl anions to fluoride anions in the synthesis gel lowers the alkalinity retarding the crystallization. As a result, the particle sizes tend to increase. The fluoride anions allow for the charge compensating of the quaternary ammonium ion of the OSDA. In the absence of alkali metals, the pores of zeolite BEA accommodates six a cluster of around ~6 TEA^+ (from TEAOH) per unit cell [38]. As the Si/Al ratio increases, the concentration of unbalanced TEA^+ cations increases. Charge conservation generally requires that framework defects be generated by breaking an Si—O—Si bond that allow for the TEA^+ to be balanced by an $Si—O^-$. The benefit of F^- anions then becomes clear as they enable the compensation of the TEA^+ cation without the need to create a framework defect [39]. Finally, the absence of alkali cations requires only a calcination step, decomposing the organic cation (TEA^+) to convert it into Brønsted acidic H-Form.

To highlight the differences of the fluoride synthesis route, a comparison to BEA synthesized in alkaline medium is made throughout this contribution. The corresponding sample ($BEA15_{OH}$) of Si/Al 15, has been largely characterized in our previous contribution, and the results are reprinted with permission from Prodinger, S.; Shi, H.; Eckstein, S.; Hu, J. Z.; Olarte, M. V.; Camaioni, D. M.; Derewinski, M. A.; Lercher, J. A., *Chem. Mater.* **2017,** 29, (17), 7255–7262. Copyright 2017 American Chemical Society.

4.3. Post-synthetic modification

To obtain a surface hydrophobized BEA zeolite, the procedure by Zapata et al. was used [18]. Briefly, the H-Form of BEA16 was suspended in toluene by using a horn sonicator. To this suspension a solution of octadecyltrichlorosilane (0.5 mmol Si/g zeolite) in toluene was added and stirred (500 rpm) at room temperature for 24 h. Upon completion the hydrophobized zeolite was separated by centrifugation (9000 rpm, 5 min) and washing of the residue with ethanol. The white powder was dried overnight at 70 °C.

4.4. Catalysis

The catalytic activity and stability of the materials was tested in aqueous phase cyclohexanol dehydration. In a typical experiment, 80 mL of 0.33 M cyclohexanol solution and 30 mg of catalyst (H-Form) was added in a Hastelloy PARR reactor, pressurized to 20 bar H_2 and heated to 170 °C. Once the set temperature was reached, stirring (670 rpm) was started and the time was recorded as time zero of the reaction. To quench the reaction, an ice-water mixture was used to rapidly cool the reactor vessel to 4 °C within 10 min. After depressurizing and opening the vessel, the reaction mixture was poured into a separation funnel and the aqueous portion was extracted five times with a total of 100 mL (20 mL per extraction) of dichloromethane. The organic phase was dried over Na_2SO_4 and analyzed using an Agilent 7890 A GC equipped with HP-5MS 25-m 0.25-um i.d. column, coupled with Agilent 5975C MS.

4.5. Inductively coupled plasma atomic emission spectroscopy (ICP-AES)

The elemental composition of the samples was determined by ICP-AES. Prior to analysis, the zeolite samples were first digested in HNO_3/HF (9:1) followed by H_3BO_3 addition.

4.6. Helium ion microscopy (HIM)

HIM images were obtained using 35 keV He ions with 0.1 pA beam current at normal incidence. Secondary electrons were detected using an Everhart–Thornley detector. For HIM imaging, a very thin layer of carbon (< 1 nm) was coated using a carbon sputter deposition system as the samples were completely insulating. The instrument resolution was 0.35 nm.

4.7. Scanning electron microscopy (SEM)

SEM images were obtained using a FEI Helios 660 FIB-SEM voltage of 10 keV and current of 1.6 nA. Si/Al analysis of the crystallites was performed with an EDAX Apollo EDS detector and TEAM software for data collection.

4.8. X–ray diffraction (XRD)

XRD patterns were collected on a Rigaku Mini Flex II bench top X–ray diffractometer using a Cu–Kα radiation of 0.154056 nm (30 kV and 15 mA). Experiments were conducted on a rotating powder sample holder in a 2θ range of 5° to 60° with a step size of 0.02°/s. All measurements were performed under ambient conditions.

4.9. N_2-physisorption

The pore size distributions were obtained by N_2-physisorption at −196 °C in a Micromeritics ASAP 2020 unit. The Tarazona NL-DFT method for N_2 in cylindrical pores without any smoothing, provided by Micromeritics was applied to assess the micropore volume. The BJH technique was used to determine the mesopore volume.

4.10. Thermogravimetric analysis (TGA)

A Netzsch STA 449C Jupiter system was used to conduct TGA and differential scanning calorimetric (DSC) analysis. A typical measurement involved 35 mg of fresh material. The material was heated to 1000 °C with a ramping rate of 5 °C/min under the flow of 50 ml/min synthetic air and 15 ml/min N_2.

4.11. Si MAS NMR

The Bloch-decay ^{29}Si MAS NMR experiments were performed using a Varian Inova 89–mm wide–bore 300 MHz NMR spectrometer and a 5 mm HXY MAS Chemagnetics style probe. The following parameters were used: a pulse width of 0.4 µs, corresponding to a 9° tip angle and 60 s of recycle delay ensured the acquisition of fully relaxed spins. The number of scans accumulated around 6000. The spinning speed was set to 5 kHz.

4.12. Al MAS NMR

The ultrahigh field ^{27}Al MAS NMR experiments were performed on a Varian-Agilent Inova 63 mm wide-bore 850 MHz NMR spectrometer. Experiments were conducted in a commercial 3.2 mm pencil type MAS probe allowing for the use of typically 15 mg of sample. In order to facilitate complete hydration of the sample, they were stored in a desiccator with saturated aqueous $Ca(NO_3)_2$ solution for 48 h. A single pulse sequence with a pulse length of 0.4 µs, corresponding to a pulse angle of 45°, was selected for acquiring each ^{27}Al MAS NMR spectrum with a recycle time of 1 s and total accumulation of 5000 scans. The spectra were acquired at a sample spinning rate of 20 kHz ± 2 Hz and were referenced to 1.5 M $Al(NO_3)_3$ in H_2O (0 ppm) using the center of the octahedral peak of solid γ-Al_2O_3 (at 13.8 ppm) as a secondary reference. For quantitative measurements, the weights of samples loaded into the MAS rotor were recorded and four spectra were acquired to check the stability of the spectrometer. The matching and tuning conditions of the RF circuit of the NMR probe were set using a network analyzer. All other experimental conditions were kept identical for all analyzed samples. In this way, the absolute peak areas normalized to the sample mass yielded a calibration factor when being plotted against known Al concentration from elemental analysis. The spectra were analyzed using the MestreNova 8.1 software package.

4.13. Infrared (IR) spectroscopy

The samples for IR measurements were prepared as self-supporting discs with a density of approximately 10 mg/cm^2. Upon loading in the IR-cell, the samples were evacuated to (1.0×10^{-7} mbar) and heated to 450 °C with a heating rate of 10 °C/min and kept at 450 °C for 1 h. Infrared spectra are recorded on a ThermoScientific Nicolete FTIR spectrometer using a MCT detector with a resolution of 4 cm^{-1}. 512 scans were accumulated for each spectrum. The spectra are normalized to the overtones and combination vibrations of the BEA lattice between 2090 and 1740 cm^{-1} [40]. The acidity was probed by dosing the base pyridine onto the sample in a controlled way. The previously activated sample (see above) was allowed to equilibrate with pyridine vapors at 0.1 mbar for one hour at 150 °C before removing all excess physisorbed pyridine via a vacuum pump (1×10^{-4} mbar). Integration of the Brønsted and Lewis peaks (1565–1515 cm^{-1} and 1470–1430 cm^{-1} respectively) and using the molar extinction coefficients determined by Maier et al. [27] along with the disc weight, the acidity could be quantified.

4.14. Liquid phase adsorption

Uptake of cyclohexanol (q) was determined using liquid ^{1}H-NMR. Typically, a 0.03 g zeolite (m) sample was immersed in 4 mL of a desired cyclohexanol solution (c_0) for 24 h at 25 °C. Quantification was accomplished adding an internal standard (maleic acid and dimethylsulfone) to the solution at equilibrium (c_e), assuming $q = V \times (c_0 - c_e) \times m^{-1}$. The uptake of water in the pores can be determined indirectly, knowing the exact micropore volume and the measured uptake of cyclohexanol.

Acknowledgment

The authors would like to acknowledge B.W. Arey for the He ion micrographs and T. Lemmon for her contribution to ICP-AES measurements, respectively. J. Hu and N. Jaeger are acknowledged for help with performing the high field NMR experiments. The high field NMR experiments and He ion microscopy were performed at the Environmental Molecular Science Laboratory, a national scientific user facility sponsored by the DOE Office of Science, Office of Biological and Environmental Research, located at Pacific Northwest National Laboratory (PNNL), a multiprogram national laboratory operated for DOE by Battelle. S.P. and M.A.D. acknowledge support by the Materials Synthesis and Simulation Across Scales (MS^3 Initiative) conducted under Laboratory Directed Research & Development Program at PNNL. H.S. and H.W. were supported by the Chemical Transformation Initiative (CTI) conducted under Laboratory Directed Research & Development Program at PNNL. J.A.L. was supported by the US Department of Energy, Office of Science, Office of Basic Energy Sciences.

Appendix A. Supplementary data

Supplementary material related to this article can be found, in the online version, at doi:https://doi.org/10.1016/j.apcatb.2018.06.065.

References

[1] A. Corma, From microporous to mesoporous molecular sieve materials and their use in catalysis, Chem. Rev. 97 (1997) 2373–2420.
[2] A. Corma, Inorganic solid acids and their use in acid-catalyzed hydrocarbon reactions, Chem. Rev. 95 (1995) 559–614.
[3] C. Zhao, J.A. Lercher, Upgrading pyrolysis oil over Ni/HZSM-5 by Cascade reactions, Angew. Chem. 124 (2012) 6037–6042.
[4] C. Zhao, D.M. Camaioni, J.A. Lercher, Selective catalytic hydroalkylation and deoxygenation of substituted phenols to bicycloalkanes, J. Catal. 288 (2012) 92–103.
[5] P.A. Jacobs, M. Dusselier, B.F. Sels, Will zeolite-based catalysis be as relevant in future biorefineries as in crude oil refineries? Angew. Chem. Int. Ed. 53 (2014) 8621–8626.
[6] Y. Liu, A. Vjunov, H. Shi, S. Eckstein, D.M. Camaioni, D. Mei, E. Barath, J.A. Lercher, Enhancing the catalytic activity of hydronium ions through constrained environments, Nat. Commun. 8 (2017) 14113.
[7] H. Shi, S. Eckstein, A. Vjunov, D.M. Camaioni, J.A. Lercher, Tailoring nanoscopic confines to maximize catalytic activity of hydronium ions, Nat. Commun. 8 (2017) 15442.
[8] R.M. Ravenelle, F. Schussler, A. D'Amico, N. Danilina, J.A. van Bokhoven, J.A. Lercher, C.W. Jones, C. Sievers, Stability of zeolites in hot liquid water, J. Phys. Chem. C 114 (2010) 19582–19595.
[9] T. Ennaert, J. Van Aelst, J. Dijkmans, R. De Clercq, W. Schutyser, M. Dusselier, D. Verboekend, B.F. Sels, Potential and challenges of zeolite chemistry in the catalytic conversion of biomass, Chem. Soc. Rev. 45 (2016) 584–611.
[10] A. Vjunov, J.L. Fulton, D.M. Camaioni, J.Z. Hu, S.D. Burton, L. Arslan, J.A. Lercher, Impact of aqueous medium on zeolite framework integrity, Chem. Mater. 27 (2015) 3533–3545.
[11] P.M. Dove, N. Han, A.F. Wallace, J.J. De Yoreo, Kinetics of amorphous silica dissolution and the paradox of the silica polymorphs, Proc. Natl. Acad. Sci. 105 (2008) 9903–9908.
[12] P.M. Dove, N. Han, J.J. De Yoreo, Mechanisms of classical crystal growth theory explain quartz and silicate dissolution behavior, Proc. Natl. Acad. Sci. 102 (2005) 15357–15362.
[13] L. Zhang, K. Chen, B. Chen, J.L. White, D.E. Resasco, Factors that determine zeolite stability in hot liquid Water, J. Am. Chem. Soc. 137 (2015) 11810–11819.
[14] S. Prodinger, M.A. Derewinski, A. Vjunov, S.D. Burton, I. Arslan, J.A. Lercher, Improving stability of zeolites in aqueous phase via selective removal of structural defects, J. Am. Chem. Soc. 138 (2016) 4408–4415.
[15] M.A. Camblor, A. Corma, S. Valencia, Spontaneous nucleation and growth of pure silica zeolite-beta free of connectivity defects, Chem. Commun. (1996) 2365–2366.
[16] M.A. Camblor, A. Corma, S. Valencia, Synthesis in fluoride media and characterisation of aluminosilicate zeolite beta, J. Mater. Chem. 8 (1998) 2137–2145.
[17] P.A. Wright, W. Zhou, J. Perez-Pariente, M. Arranz, Direct observation of gowth defects in zeolite beta, J. Am. Chem. Soc. 127 (2005) 494–495.
[18] P.A. Zapata, J. Faria, M.P. Ruiz, R.E. Jentoft, D.E. Resasco, Hydrophobic zeolites for biofuel upgrading reactions at the liquid-liquid interface in water/oil emulsions, J. Am. Chem. Soc. 134 (2012) 8570–8578.
[19] S. Prodinger, H. Shi, S. Eckstein, J.Z. Hu, M.V. Olarte, D.M. Camaioni, M.A. Derewinski, J.A. Lercher, Stability of zeolites in aqueous phase reactions, Chem. Mater. 29 (2017) 7255–7262.
[20] P. Scherrer, Bestimmung der Größe und der inneren Struktur von Kolloidteilchen mittels Röntgenstrahlen Nachrichten von der Gesellschaft der Wissenschaften zu Göttingen, Mathematisch-Physikalische Klasse 2 (1918) 98–100.
[21] R. Gounder, A.J. Jones, R.T. Carr, E. Iglesia, Solvation and acid strength effects on catalysis by faujasite zeolites, J. Catal. 286 (2012) 214–223.
[22] A. Vjunov, J.L. Fulton, T. Huthwelker, S. Pin, D. Mei, G.K. Schenter, N. Govind, D.M. Camaioni, J.Z. Hu, J.A. Lercher, Quantitatively probing the Al distribution in zeolites, J. Am. Chem. Soc. 136 (2014) 8296–8306.
[23] A.E.W. Beers, J.A. van Bokhoven, K.M. de Lathouder, F. Kapteijn, J.A. Moulijn, Optimization of zeolite Beta by steaming and acid leaching for the acylation of anisole with octanoic acid: a structure-activity relation, J. Catal. 218 (2003) 239–248.
[24] M. Müller, G. Harvey, R. Prins, Quantitative multinuclear MAS NMR studies of zeolites, Microporous Mesoporous Mater. 34 (2000) 281–290.
[25] H.-M. Kao, Y.-C. Chen, ^{27}Al and ^{19}F solid-state NMR studies of zeolite H-β dealuminated with ammonium hexafluorosilicate, J. Phys. Chem. B 107 (2003) 3367–3375.
[26] G.L. Woolery, L.B. Alemany, R.M. Dessau, A.W. Chester, Spectroscopic evidence for the presence of internal silanols in highly siliceous ZSM-5, Zeolites 6 (1986) 14–16.
[27] S.M. Maier, A. Jentys, J.A. Lercher, Steaming of zeolite BEA and its effect on acidity: a comparative NMR and IR spectroscopic study, J. Phys. Chem. C 115 (2011) 8005–8013.
[28] T. Blasco, M.A. Camblor, A. Corma, P. Esteve, J.M. Guil, A. Martínez, J.A. Perdigón-Melón, S. Valencia, Direct synthesis and characterization of hydrophobic aluminum-free Ti−Beta zeolite, J. Phys. Chem. B 102 (1998) 75–88.
[29] C.A. Fyfe, J.M. Thomas, J. Klinowski, G.C. Gobbi, Magic-angle-spinning Nmr (Mas-Nmr) spectroscopy and the structure of zeolites, Angew. Chem. Int. Ed. Engl. 22 (1983) 259–275.
[30] G. Engelhardt, D. Michel, High-Resolution Solid-State Nmr of Silicates and Zeolites, John Wiley & Sons, Australia, 1987 Limited.
[31] S. Prodinger, A. Vjunov, J.Z. Hu, J.L. Fulton, D.M. Camaioni, M.A. Derewinski, J.A. Lercher, Elementary steps of faujasite formation followed by in situ spectroscopy, Chem. Mater. 30 (2018) 888–897.
[32] C. Zhao, J. He, A.A. Lemonidou, X. Li, J.A. Lercher, Aqueous-phase hydrodeoxygenation of bio-derived phenols to cycloalkanes, J. Catal. 280 (2011) 8–16.
[33] U.A. P, d.J. Ernesto, D. Jairton, Turnover numbers and soluble metal nanoparticles, ChemCatChem 3 (2011) 1413–1418.
[34] P.A. Zapata, Y. Huang, M.A. Gonzalez-Borja, D.E. Resasco, Silylated hydrophobic zeolites with enhanced tolerance to hot liquid water, J. Catal. 308 (2013) 82–97.
[35] S. Prodinger, M.A. Derewinski, Y. Wang, N.M. Washton, E.D. Walter, J. Szanyi, F. Gao, Y. Wang, C.H.F. Peden, Sub-micron Cu/SSZ-13: synthesis and application as selective catalytic reduction (SCR) catalysts, Appl. Catal., B 201 (2017) 461–469.
[36] F. Fajula, L. Moudafi, R. Dutartre, F. Figueras, Influence of the morphology of the particles on the thermal-stability of offretite, Nouv. J. Chim. 8 (1984) 207–211.
[37] J.M. Newsam, M.M.J. Treacy, W.T. Koetsier, C.B. Degruyter, Structural characterization of zeolite-beta, Proc. R. Soc. Lond. Ser. A 420 (1988) 375–405.
[38] T. Ikuno, W. Chaikittisilp, Z. Liu, T. Iida, Y. Yanaba, T. Yoshikawa, S. Kohara, T. Wakihara, T. Okubo, Structure-directing behaviors of tetraethylammonium cations toward zeolite beta revealed by the evolution of aluminosilicate species formed during the crystallization process, J. Am. Chem. Soc. 137 (2015) 14533–14544.
[39] J.L. Guth, H. Kessler, R. Wey, New route to pentasil-type zeolites using a non alkaline medium in the presence of fluoride ions, Stud. Surf. Sci. Catal. 28 (1986) 121–128.
[40] A. Jentys, J.A. Lercher, IR study of the adsorption of benzene on HZSM5, Stud. Surf. Sci. Catal. 46 (1989) 585–594.